Icosahedral silicon boride: A potential hybrid photovoltaic-thermoelectric for energy harvesting

Kang Xia [1,2] Qun Chen,[2] Hao Gao,[2] Xiaolei Feng,[3,4] Jianan Yuan,[2] Cong Liu,[2] Simon A. T. Redfern [5] and Jian Sun [2,*]

[1]*Department of Applied Physics, College of Science, Nanjing Forestry University, Nanjing 210037, China*

[2]*National Laboratory of Solid State Microstructures, School of Physics and Collaborative Innovation Center of Advanced Microstructures, Nanjing University, Nanjing 210093, China*

[3]*Center for High Pressure Science and Technology Advanced Research, Beijing 100094, China*

[4]*Department of Earth Sciences, University of Cambridge, Downing Street, Cambridge CB2 3EQ, United Kingdom*

[5]*Asian School of the Environment and School of Materials Science and Engineering, Nanyang Technological University, Singapore 639798*

(Received 15 February 2021; accepted 19 October 2021; published 29 November 2021)

Boron-rich compounds have attracted significant attention due to their promising and diverse physical properties, which include ultrahardness, resistance to oxidation and corrosion, and even superconductivity. Here, using a crystal structure search method based on first-principles calculations, we find a boron-rich silicon compound SiB_{12} that is stable under moderate pressure of around 20 GPa, and which we predict is recoverable to ambient pressure. This silicon boride, with space group *Pnnm*, is structurally related to the γ-B_{28} boron phase. Specifically, the SiB_{12} structure is formed by replacing the B_2 pairs in γ-B_{28} with silicon atoms. Our calculations show that this *Pnnm* SiB_{12} phase exhibits good thermal stability at moderate pressures above 20 GPa and temperatures to 900 K. We suggest this structure has dynamic stability at ambient pressure and remains stable to temperatures as high as 2000 K. Impressively, this SiB_{12} phase possesses good light absorption and thermoelectrical properties, which are enhanced by its small and indirect band gap, doubly degenerate bands, and low lattice thermal conductivity. Our predictions should stimulate further investigations of this class of boron-rich semiconductors, especially in view of their superior photovoltaic and thermoelectric properties which may be beneficial in energy applications.

DOI: 10.1103/PhysRevMaterials.5.115402

I. INTRODUCTION

Tremendous efforts have been made to improve the conversion efficiency of photovoltaics, for effective use of solar energy for electricity generation. These have included the development of new photovoltaic materials with unique conversion characteristics [1,2]. However, such photovoltaic materials typically cannot convert the long-wavelength solar radiation, with energy less than the band gap. Absorption and energy conversion associated with electron transitions across an indirect gap require phonon assistance and so will also result in generation of a certain amount of heat. Both of these two processes significantly limit the solar conversion efficiency at long wavelengths [3]. Thermoelectric materials have been proposed and designed to overcome these limitations. The thermoelectric effect directly converts heat, from the infrared portion of incident insolation, to electricity [4,5]. It may be possible to overcome shortcomings of photovoltaic conversion at long wavelengths by combining photovoltaic and thermoelectric properties in materials. Indeed, photovoltaic and thermoelectric hybridization has been proposed as a strategy for developing efficient energy conversion in the effort to switch to sustainable and clean energy sources for the future [6,7].

Nanostructure heterojunctions provide a route to develop hybrid photovoltaic-thermoelectric system for solar cell devices [8,9]. Such systems require narrow band gaps (E_g) and high carrier mobilities. These are essential, not only to increase the photon-absorbing efficiency of electricity generation, but also to improve the thermoelectric quality factor for heat conversion [5,10,11]. For instance, a typical cubic GaAs (c-GaAs) cell has a direct E_g of around 1.5 eV. It has an absorption coefficient varying from 10^4 cm^{-1} at a photon energy of 1.6 eV to around 10^6 cm^{-1} at 3.0 eV [12]. The conversion efficiency can reach about 28.8% for solar energy, which is close to the Shockley-Queisser limit of around 30% [10]. On the other hand, the extremely low thermal conductivity (κ_L) of complex semiconductors such as half-Heusler and clathrate structures [13–16], is found to be a key factor in limiting the phonon heat transport in their crystalline lattices. The dimensionless figure of merit (ZT) is an indication of the effectiveness of this heat conversion efficiency. Therefore, complex semiconductors with both narrow band gap and low lattice thermal conductivity provide a possible approach to develop hybrid photovoltaic-thermoelectric materials with good total solar energy conversion efficiency.

Elemental boron has three valence electrons and, as a metalloid, is located mid-way between the metallic and nonmetallic elements on the periodic table. The bonding characteristics of boron-rich compounds typically do not follow conventional valence rules and boron networks may show complex atom-bond connectivity, with mixtures of double and triple connections. Boron may also form networks which combine polyhedral units such an octahedra or cubes composed solely of boron. Boron-rich compounds favor the formation of icosahedral B_{12} units. Such structural frameworks can result in a diverse range of semimetallic or metallic allotropes.

*Corresponding author: jiansun@nju.edu.cn

These include the orthorhombic τ boron, the high-pressure semiconducting γ-$B_{28,}$ and the superconducting α-Ga phases [17–19]. Antiferromagnetism has been reported to exist in two-dimensional (2D) boron sheets, which also display massless Dirac cones in their band structures [20,21]. Additionally, by combination and doping with a range of other elements, structures composed of B_{12} icosahedra may be engineered to exhibit interesting and useful physical properties, including superhardness, superconductivity, topological semimetallicity and 2D metallicity [22–25]. In particular, impurity doping in α-B and β-B forms of boron can be used to modify their E_g by changing bonding interactions [26]. The corresponding boron-rich semiconductors typically show high mobility and are found to display the thermoelectric effect, but reports of the maximum ZT achieved are around 0.17 at high working temperatures of 1200°C [26].

The application of high pressures is known to almost invariably result in the modification of materials' structures and properties and many novel structures have been successfully discovered by searching in the high-pressure realm. For example, pressure may be used as a route to obtain metastable metallic or semiconducting silicon borides [27], novel silicon allotropes [28–30], and thermoelectric materials [31–33]. However, to the best of our knowledge, the use of high pressure in arriving at borides with enhanced photovoltaic and thermoelectric performance has not been previously reported. Here, therefore, we explore the combination of silicon, which plays a well-established and important role in solar cell applications [28,29], with boron in the context of the search for a high-performance combined photovoltaic and thermoelectric material. We have explored the effects of silicon doping on the complex structures and properties of materials formed from boron icosahedra. We successfully predict a metastable silicon boron-icosahedral compound, SiB_{12}, which is energetically favored under high pressure and remains quenchable to ambient conditions. Our calculations show that our predicted SiB_{12} phase has good thermal and dynamic stability to temperatures as high as 2000 K. In addition, and importantly, we find it is an intrinsic semiconductor with both good absorption and thermoelectric performances.

II. COMPUTATIONAL DETAILS

To search for novel silicon-boron compounds we have adopted a machine-learning and graph theory aided crystal structure search method [34–36]. This method has previously been successfully applied to many systems, and has had notable success in the discovery of a new T-graphene intercalation compound [37], helium compounds [38–40], and metal pentazolate salts [41,42]. To enhance efficiency, here, we treat the B_{12} icosahedral motif as a basic molecular unit during the structure searching. In our first-principles calculations, we adopted the Perdew-Burke-Ernzerhof functional with the generalized-gradient approximation (GGA–PBE) [43] and projector-augmented wave (PAW) method [44] implemented in the VASP code [45]. Considering the short distances between icosahedral boron atoms, we chose the hard PAW-PBE potential to optimize the structure and calculate the total energy. A kinetic cutoff energy of 1050 eV together with a k-mesh spacing of $2\pi \times 0.03\,\text{Å}^{-1}$ was used. To obtain the Gibbs free energy, we have performed computationally intensive phonon calculations based on the quasiharmonic approximation (QHA) employed in the PHONOPY-QHA script [46,47]. The temperature-dependent harmonic phonon energy can be evaluated based on the second-order or harmonic force constants. The unique minimum $G(T,\ P)$ at pressure P and varying temperature T is given by $G(T,P) = \min_V [U(V) + F_{\text{phonon}}(T;V) + PV]$. We included the conformational entropy and the electronic total energy contribution by the phonon free energy F_{phonon} and the $U(V)$ part, respectively. We take into consideration of the zero-point energy and temperature-dependent phonon free energy. By charting the change in volume V expansion with T, we can calculate the minimum Gibbs energy. We analyzed the covalent bonding characteristics as well as the noncovalent interactions (NCIs) by calculating the electron localization functional [48] using CRITIC2 calculations [49,50] combined with VASP. We visualized the steric NCIs using Visual Molecular Dynamics software [51]. We estimated the intrinsic hardness and strength by deforming our computed structures under a simulated Vickers indentation test [52,53]. Specifically, we compressed the structure along the [001] direction. The normal stress (σ_{zz}) has to uniformly satisfy the criterion for Vickers indenter, that is, $\sigma_{zz} = \sigma_{zx} \tan\varphi$ ($\varphi = 68^\circ$) [where, σ_{zx} represents the stress tensor component induced by shearing within the (001) plane along the [100] direction] while the other five independent tensor components remain negligible (<0.05 GPa). By loading continual strains in the shearing plane (001), we relaxed the resulting structure with convergence criteria such that convergences of the total energy were $<10^{-6}$ eV between the electronic self-consistent loops and force <0.005 eV/Å on each atom. The shear stress tensor components σ_{ij} are given by $\sigma_{ij} = \frac{1}{V}\frac{\partial E}{\partial \epsilon_{ij}}$, where ϵ_{ij} is the one nonzero strain. The other strain components reach zero after full relaxation. Here, E and V represent the total energy and optimized cell volume. To obtain accurate electronic structures and related band gaps, we performed all-electron calculations modified by the Becke-Johnson (mBJ) potential [54] implemented in the WIEN2k program [55]. We employed the linearized-augmented plane-wave method. We further estimated the optical absorption spectra in the visible-light range. We calculated phonon dispersion curves using the PHONOPY code [47]. Moreover, we performed the *ab initio* molecular dynamics (AIMD) simulations [56,57] and self-consistent phonon (SCPH) calculations [58]. We perform AIMD and phonon calculations for 256 atoms within a $(2 \times 2 \times 2)$ supercell. The time for each AIMD step was 1 femtosecond. We use the Langevin thermostat [59–61] to run N_PT and N_VT dynamics. The Parrinello-Rahman barostat was applied to achieve the N_PT ensemble by relaxing the cell volume and shape [56,62]. Employing density functional perturbation theory as implemented in the VASP code, we calculated force constants in real space, which are necessary to evaluate the frequency of Raman-active modes at the Γ point. Particularly, to estimate the anharmonic phonon dispersion at finite temperatures, we used the HIPHIVE package [63] to extract high-order force constants from the AIMD trajectory. In the original implementation of SCPH in HIPHIVE code, the classical limit of normal mode amplitudes was used. Here, we performed stochastic sampling based on nonapproximate distribution [64] so that anharmonic phonons at low temperatures are accessible. By employing the BOLTZTRAP code [65], we also

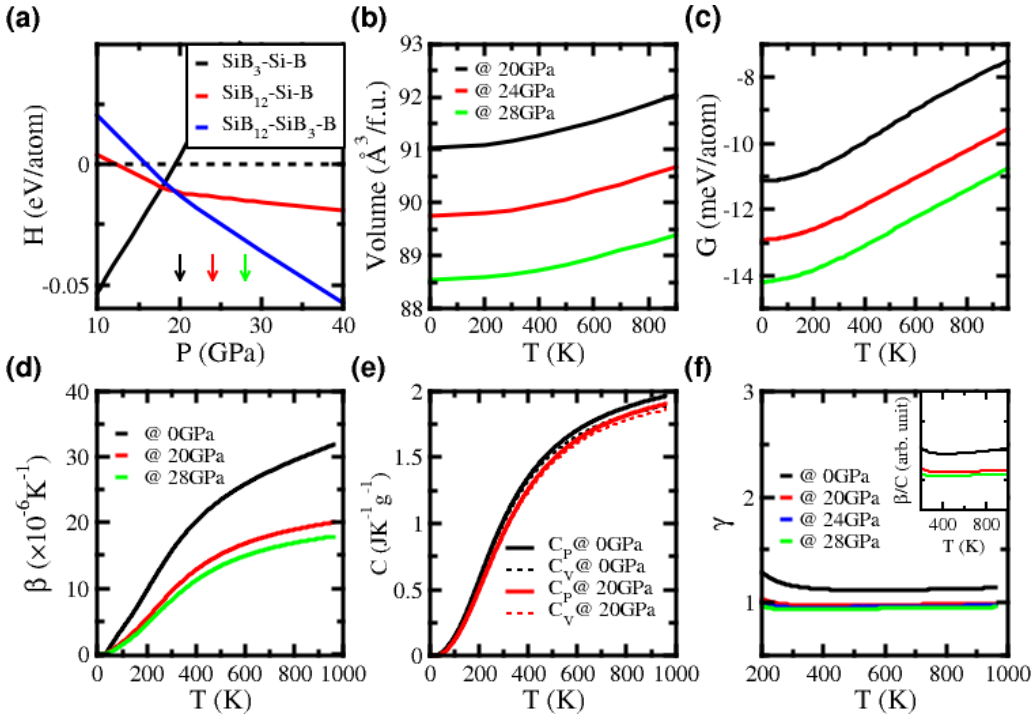

FIG. 1. (a) The enthalpy (H) difference between the *Pnnm* SiB_{12} structure and a mixture of β-Sn II-type silicon and γ boron, or a mixture of SiB_3 and γ boron, under moderate pressures P of 10–40 GPa. The dashed base line in (a) is the enthalpy base line for the equivalent mixture of elemental silicon and boron. (b)–(f) Thermal properties of SiB_{12} across temperature-pressure space using the QHA. (b) The unit cell volume expansion with temperature T at pressures of 20, 24, and 28 GPa. (c) The estimate of the difference in Gibbs free energy (G) of SiB_{12} relative to the equivalent Si-II and γ-B_{28} mixture at different temperatures with constant pressures. (d) Volumetric thermal expansion coefficient β, and (e) heat capacity C, and (f) thermodynamics Grüneisen parameter γ versus T. The black, red, and green solid lines in (b) and (c) represents thermal properties at pressures of 20, 24, and 28 GPa respectively. The ratio of β/C is the inset in (f).

estimated the thermoelectric properties. The electronic transport calculations depend on the WIEN2k electronic structures. We solved the Boltzmann transport equation for phonons by using the SHENGBTE program [66]. Running the third-order script with VASP, we obtained the third-order anharmonic interatomic force constants (IFCs), which are necessary for the calculations of lattice thermal conductivity and related phonon scattering properties. We generated an irreducible set of displacements for the $(2 \times 2 \times 2)$ supercell and up-to-sixth-neighbor interactions. Thousands of VASP POSCAR files are created. We perform the density functional theory (DFT) IFC matrix calculations using VASP and reconstructed them as third-order IFCs.

III. RESULTS AND DISCUSSIONS

A. Thermal stability and properties

We investigated the complexation of icosahedral boron motifs with silicon atoms by employing a molecular evolutionary method [34,42]. We then calculated the enthalpy of formation (ΔH_f), which is defined as $\Delta H_f = [H(SiB_x) - H(Si) - xH(B)]/(x+1)$, for resulting phases. Here, x is the boron concentration, $H(SiB_x)$ represents the enthalpy for one SiB_x formula unit (f.u.), while H(Si) and H(B) is the enthalpy for elemental silicon and boron. The α-B, γ-B_{28}, diamondlike d-Si, β-Sn structured Si-II phases and SiB_3 compound, were used for these calculations at the appropriate conditions [18,27,29]. The ΔH_f for silicon boride SiB_{12} was found to be lower than that of the previously reported SiB_3 structure [27] at pressures of approximately 18 GPa or more [Fig. 1(a)]. The enthalpy of the SiB_{12} structure is predicted to be lower than that of a mixture of the SiB_3 and boron end members at pressures above 16 GPa, as indicated from $\Delta H_f = [H(SiB_{12}) - H(SiB_3) - 9H(B)]/13$, shown as the solid blue line in Fig. 1(a). Therefore, we conclude that this icosahedral SiB_{12} phase is enthalpically stable at these moderate pressures and will appear in the silicon-boron phase diagram as a function of pressure.

Pressure of more than 20 GPa can be obtained experimentally using the multianvil large volume press or (to higher pressures) diamond anvil cells, suggesting the possibility of experimental synthesis. However, temperature usually affects synthesis route and product stability and even though it may be possible to synthesize high-pressure compounds, they may subsequently decompose upon compression. To investigate the thermal stability of SiB_{12}, we have performed challenging and computationally intensive first-principles calculations of the Gibbs free energy of SiB_{12} using the QHA, and compared its stability against mixtures of elemental silicon and boron. At pressures above 20 GPa, the black solid line in Fig. 1(a) shows that SiB_3 is enthalpically unstable, decomposing into elemental mixtures. We have therefore calculated the Gibbs free energy at constant pressure [20, 24, and 28 GPa, pointing as black, red, blue arrows respectively in Fig. 1(a)] and temperature $G(T, P)$ for the SiB_{12} structure, relative to mixtures of Si-II and γ-B_{28}, the stable phases under

the conditions of interest. The formation Gibbs free energy is given as $\Delta G_f = [G(SiB_{12}) - G(Si) - 12G(B)]/13$, where $G(SiB_{12})$ represents the Gibbs free energy at constant pressure and temperature for one formula unit of SiB_{12}. Moreover, we have evaluated the thermal expansion coefficient β, heat capacity at constant pressure C_P, and Grüneisen parameter γ by expanding thermal properties via the QHA method.

We introduce the volume dependence of phonon frequencies to take account of anharmonic effects. At constant pressure, the Gibbs free energy can be considered by expanding the cell volume on increasing temperature from 0 to 900 K, as shown by the black solid-dot lines in Supplemental Material (SM) [67] Fig. S1. Using the QHA method implemented in PHONOPY-QHA, we obtain the equilibrium cell volume as a function of temperature [Fig. 1(b)] in accordance with the red solid-dot lines in SM Fig. S1. We then compare the unique minimum $G(T, P)$ of the SiB_{12} structure against that of Si-II and γ-B_{28} mixtures at pressures of 20, 24, and 28 GPa and a function of temperature [Fig. 1(c)]. The Gibbs free energy difference, ΔG_f, between SiB_{12} and the mixture of elementary Si-II and γ-B_{28} substances increases from around -11 to -7.5 meV/atom with increasing temperature at 20 GPa, and from -14 to -11 meV/atom at 28 GPa. These negative Gibbs formation energies, ΔG_f, indicate that SiB_{12} is expected to be thermally stable at temperatures up to at least 900 K. We estimated the temperature-dependent electron free energy contribution to be around 0.004, 5.000, and 3.000 meV/atom at most for SiB_{12} structure, Si-II, and γ-B_{28} substances, respectively. From these data, we can see that the electrons from silicon atoms make the main contribution to the electron free energy. However, since the SiB_{12} structure has a small silicon concentration ($\sim$0.077), it should have a small contribution ($\sim$0.385 meV/atom) to the Gibbs free energy. Therefore, we neglect the temperature-dependent electron free energy. Theoretically, we suggest the SiB_{12} structure will not decompose into simpler compounds or elemental end members even at high temperatures.

From the change in thermodynamic properties with temperature, we have obtained the volumetric thermal expansion coefficient β, heat capacity at constant volume C_V, and thermodynamic Grüneisen parameter $\gamma = V\beta B_T/C_V$ as a function of T [Figs. 1(d)–1(f)]. Pressure is found to decrease β and γ. The difference between heat capacity at constant pressure C_P and C_V is small [Fig. 1(e)]. We find that the ratio of thermal expansion β to heat capacity C [Inset of Fig. 1(f)] is independent of temperature, consistent with constant γ [Fig. 1(f)]. All these thermal properties may be used to characterize the thermally stability of SiB_{12} upon synthesis.

B. Structure and bonding characteristics

The new stoichiometric SiB_{12} structure possesses space group *Pnnm* and contains two SiB_{12} units within its unit cell. The structural parameters are listed in SM Table SI. Silicon atoms occupy interstitial sites between the boron icosahedra, resulting in the formation of relatively open silicon channels along the [010] direction. We have calculated the Bader charge [68] for the SiB_{12} structure using the PAW method employed in the VASP code, as listed in SM Table SI. We find ionic interactions exist between Si and the B_{12} cluster, similar to that seen in NaCl-type ionic γ boron [18]. However, the boron atoms at Wyckoff-position *B(2)* and *B(3)* attract $0.1369e$ and $0.2144e$, respectively. Each silicon atom delivers $1.3249e$ charge transferred to the B_{12} unit, which is estimated to be over twice as much as charge transfer ($0.5e$) between B_2 pairs and the B_{12} unit in γ boron. This difference originates from the higher electronegativity of boron than silicon, so that silicon easily donates electrons. The charge transfer between Si and the B_{12} unit means that *Pnnm* SiB_{12} can be considered an ioniclike compound, $Si^{1.3+}(B_{12})^{1.3-}$.

By computing the electron localization function (ELF), we further analyzed the electron localization and bonding characteristics of this structure. Strong covalent bonds exist between boron atoms at the polar sites [B_P, pink colored in Fig. 2(a)] of the B_{12} icosahedra, as seen by the high ELF value (about 1.0) shown in Fig. 2(b) in the positions of these bonds. The B_P atoms are connected to adjacent boron icosahedra at a relatively short distance of around 1.621 Å, which we note is shorter than that of the equivalent distance in γ-B_{28} (1.80 Å) [18]. Strong electron density is found to be located around the B_P-adjacent boron atom [green with yellow-crossing mark in Fig. 2(a)]. The light blue contours with low ELF values indicate the weak electron localization.

However, our ELF analysis cannot inform about the NCIs for the extremely low electron density (ρ). Nevertheless, the CRITIC2 program has been developed to solve such a problem [50]. By performing CRITIC2 calculations, weak electron interactions have been successfully studied in many systems, including inorganic perovskites [69], polymorphic molecular crystals [70], and van der Waals materials [71]. NCIs can be analyzed by dividing the low electron density gradient $\nabla\rho$ by $\rho^{4/3}$, where ρ is the electron density obtained from the DFT electron wave functions. The key index, namely, reduced density gradient (RDG, s) is defined as $s = \frac{1}{2(3\pi^2)^{1/3}}\frac{|\nabla\rho|}{\rho^{4/3}}$. Therefore, we can investigate the NCIs between the boron icosahedra and interstitial silicon atoms using CRITIC2 calculations. The very weak NCIs, such as van der Waals interactions, appear as peaks with $s = 0$ located at $\rho \approx 0.0$ arbitrary units (arb. units) [Fig. 2(c)]. We use the sign of the second electron-density Hessian eigenvalue (λ_2) to distinguish repulsive (positive λ_2) and attractive (negative λ_2) NCIs with low-S saddles appearing at low ρ values of around 0.05 and 0.1 arb. units. Figure 2(d) shows the steric 3D counter plots. The red and blue counter plots exhibit the repulsive and attractive interactions, respectively. The extremely weak 3D NCIs show up as the green "grainlike" objects in the counter plots. Therefore, we suggest that weak chemical interactions exist between silicon atoms and boron icosahedra.

Interestingly, we observe ringlike noncovalent interactions, albeit with low electron density. The covalent bonding in boron icosahedra explains its good thermal and dynamical stability up to high temperatures. The covalent bonds between polar boron atoms may aid resistance during the Vickers indentation process.

C. Dynamical stability at temperatures

We further tested the dynamical stability of SiB_{12} at ambient pressure and finite temperatures by carrying out calculations of the phonon dispersion relations of the stable

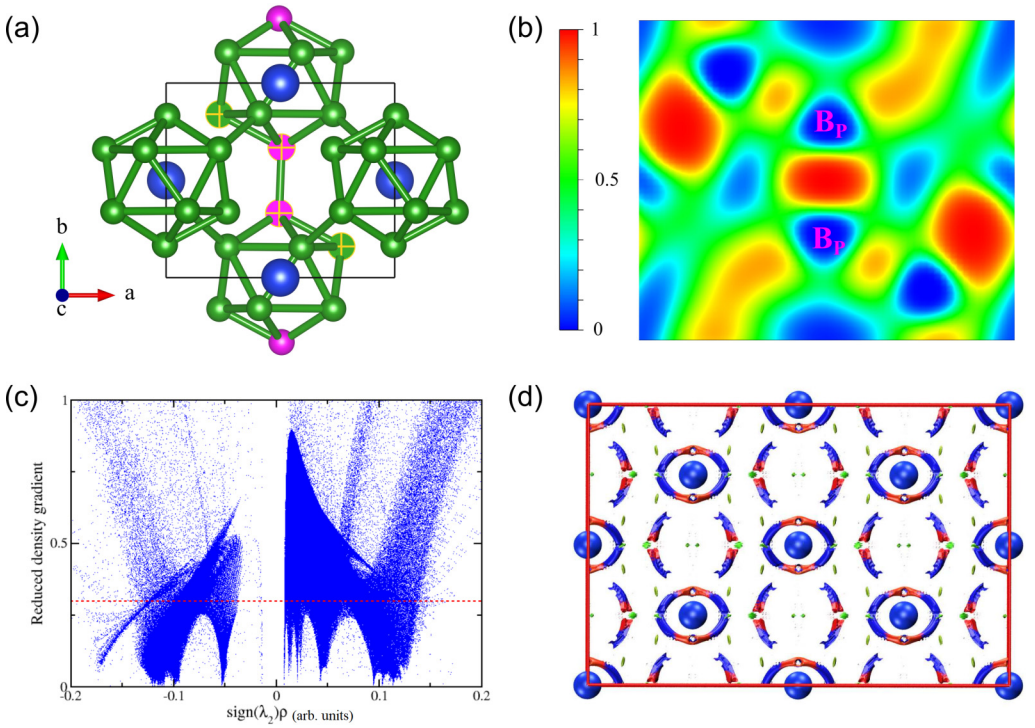

FIG. 2. (a) Crystal structure for SiB_{12} at 0 GPa (green for boron, and blue for silicon atoms). (b) The ELF map depicted by the plane cutting through boron atoms with yellow-crossing marks in (a). (c) The calculated two-dimensional (2D) graphic of noncovalent interactions (NCIs) by the reduced density gradient (RDG, s). (d) Three-dimensional (3D) NCIs counter plots with the isovalue $s = 0.3$ arb. units as red dashed line shown in (c). To clearly visualize the NCIs regions, we did not draw the boron icosahedra in (d).

phase. No imaginary phonon branches were found, indicating the dynamical stability of the structure at 0 GPa and 0 K [left panel of Fig. 3(a)]. High-frequency internal optic phonons, existing around 1200 cm^{-1} [red curves in Fig. 3(a)] show little dispersion across the entire Brillouin zone. This mode corresponds to opposing vibrational motions of B_P atoms along the [010] direction, as indicated by the red arrows in the inset structure of Fig. 3(a). By calculating the partial phonon density of states (PDOS) projected on different atoms, the peak appearing at around 1200 cm^{-1} can be wholly attributed to the vibration of B_P boron atoms, as shown in the right panel of Fig. 3(a). Additionally, the PDOS calculations show that the vibrational modes at frequencies below 1000 cm^{-1} mainly come from the motions of nonpolar boron (B_{NP}) atoms. We further calculate the frequency of Raman-active modes in the *Pnnm* SiB_{12} structure under different pressures. The frequency for Raman-active modes $A_g + B_{1g} + B_{2g} + B_{3g}$ increases with compression, as shown in Fig. 3(b). In particular, the strongest A_g Raman-active mode, shown as the red dotted line, is well separated from the others and may serve as a useful diagnostic feature in any experimental high-pressure structural assessment.

We note that finite temperatures usually induce anharmonic effects on a crystal's phonon dispersion curves and may modify the structural stability or a particular phase [72–74]. To confirm the thermal dynamic stability of our SiB_{12} structure at finite temperatures, we have made efforts to obtain the higher-order force constants and calculate the entire phonon spectra. Using the SCPH method [63], we predict the phonon curves at 0 GPa and room temperature [Fig. 3(c)]. An increase from 0 K to room temperature is found to enhance the atomic vibration and results in phonon hardening. We have performed AIMD calculations of this phase at ambient pressure and high temperatures, up to 2000 K, as shown in Figs. 3(d)–3(i). Alongside these AIMD simulations, we have used a three-step strategy to obtain the anharmonic force constants as a function of increasing temperature. Firstly, we perform AIMD simulations in the N_PT ensemble for 12 picosecond (ps) time steps, adopting every equilibrium cell. Secondly, with these cell constraints, we employ the N_VT ensemble during another 12 ps AIMD simulations. Lastly, we can extract force constants and fit the phonon dispersion curves corresponding to high temperature conditions.

We have extracted the temperature (T), pressure (P), and lattice parameter (a, b, and c) changes during the AIMD simulation time steps (t), as shown in SM Figs. S2 and S3. After 2 ps of AIMD simulations, the SiB_{12} structure is found to reach all equilibrated states in the N_PT ensemble under different temperatures. We have used the radial distribution function ($g(r)$) to analyze the atomic bonding information. The first sharp peak for $g(r)$ appears at an interatomic distance, r, of around 1.75 Å, as shown in Figs. 3(d)–3(f). This bond length is close to the averaged length value around 1.787 Å for boron-boron bonds in the boron icosahedron at 0 GPa and 0 K. Thus, we conclude that the boron icosahedron remains intact at high temperature up to 2000 K at ambient pressure. The averaged cell volume expands with loading temperatures during AIMD simulations. Specifically, the averaged unit-cell volume reaches to 190.3, 191.4, and 198.8 $Å^3$ at temperatures of 300, 1000, and 2000 K, respectively.

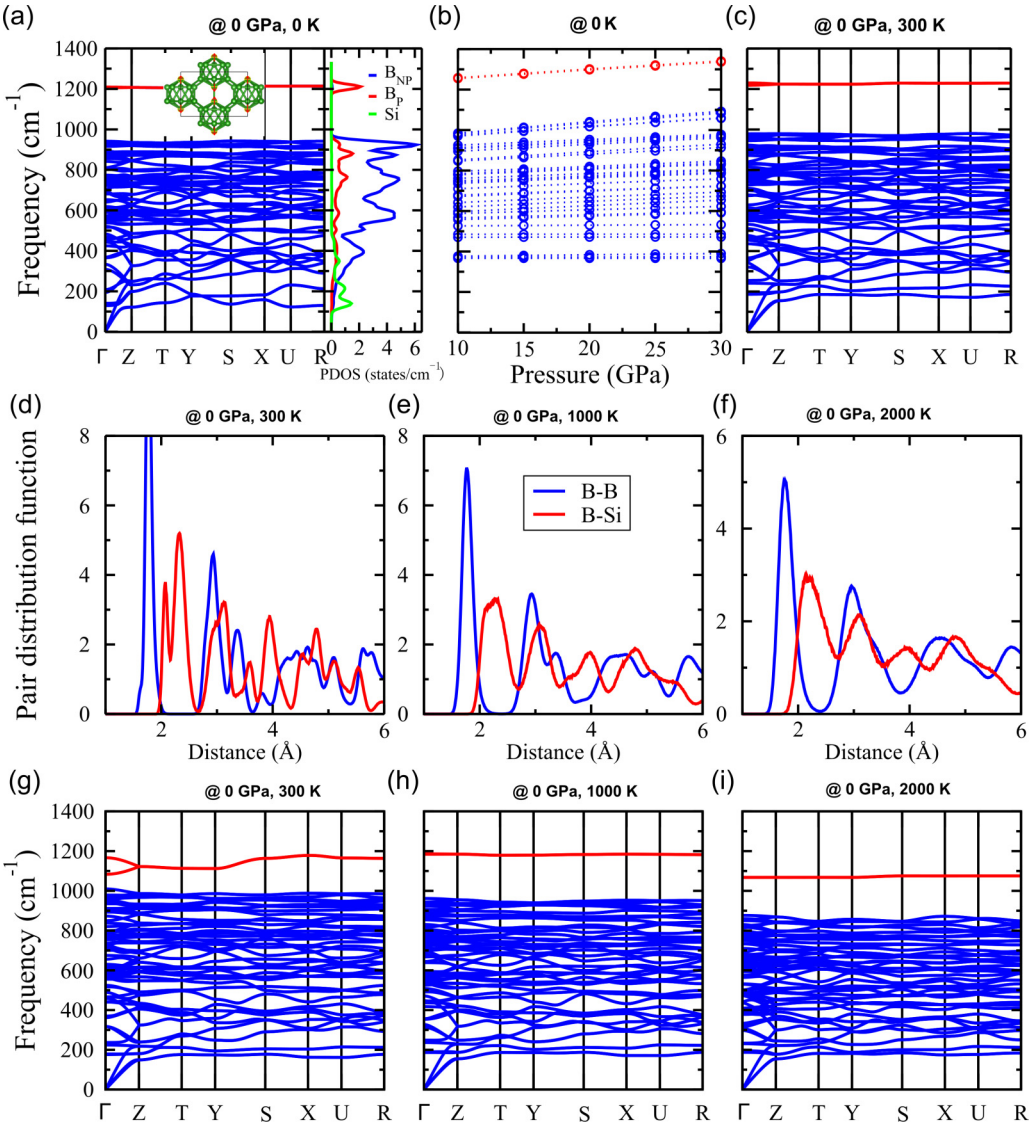

FIG. 3. Dynamical and thermal stability of SiB_{12} at 0 GPa and finite temperatures. (a) The harmonic phonon dispersion spectra (left panel) and partial phonon density of state (PDOS, right panel) at 0 GPa and 0 K. (b) The evolution for theoretical frequencies of Raman-active modes ($A_g + B_{1g} + B_{2g} + B_{3g}$) as a function of pressures. (c) The anharmonic phonon curves calculated by the SCPH method at 0 GPa and 300 K. (d)–(f) The broadened pair distribution functions and (g)–(i) thermal phonon spectra for SiB_{12} structure, by performing the AIMD simulation at temperatures from 300 to 2000 K. Red curves in (a)–(c) represent the phonon dispersion of the highest frequency. We clearly observe the B_p opposite atomic vibration behavior by hiding the silicon atoms, as the inset of (a) shows.

We further employ the technique of temperature-dependent effective potential [63,75] into AIMD simulations in the $N_V T$ ensemble [57], as Figs. 3(g)–3(i) exhibit. The phonon spectra at 300 K fitting from AIMD simulation, agree with self-consistent results as the blue curves in Fig. 3(c) show. We note, however, that the highest vibration frequency along Γ-*R* line appears to separate. The reason may be that the sampling method we use during our room-temperature AIMD simulations is unable to reflect the quantum vibration behavior [58]. Obviously, phonon curves bunch to lower frequencies as temperature is increased to 2000 K with an increase of around 1.6% of the unit-cell volume, compared to the structure at 0 K, as seen from Fig. 3(i). Phonons soften on increasing temperature as the covalent boron-to-boron interaction weakens during the volume expansion on heating. Nevertheless, all AIMD simulations show positive real phonon dispersion, demonstrating that the *Pnnm* SiB_{12} structure has very good thermal and dynamic stability at high temperatures. This suggests that the silicon boride SiB_{12} structure can be quenchable to ambient conditions once synthesized, and may stimulate experimentalists to obtain such metastable materials recovered from extremely high temperature and pressure studies.

D. Stress response to the strain deformation

Icosahedral boron is a well-known component of incompressible allotropes of bulk boron [18,19] which typically display super hardness. To study the mechanical properties of orthorhombic *Pnnm* SiB_{12}, we have calculated the elastic constants at 0 GPa, as listed in SM Table SI. We find this

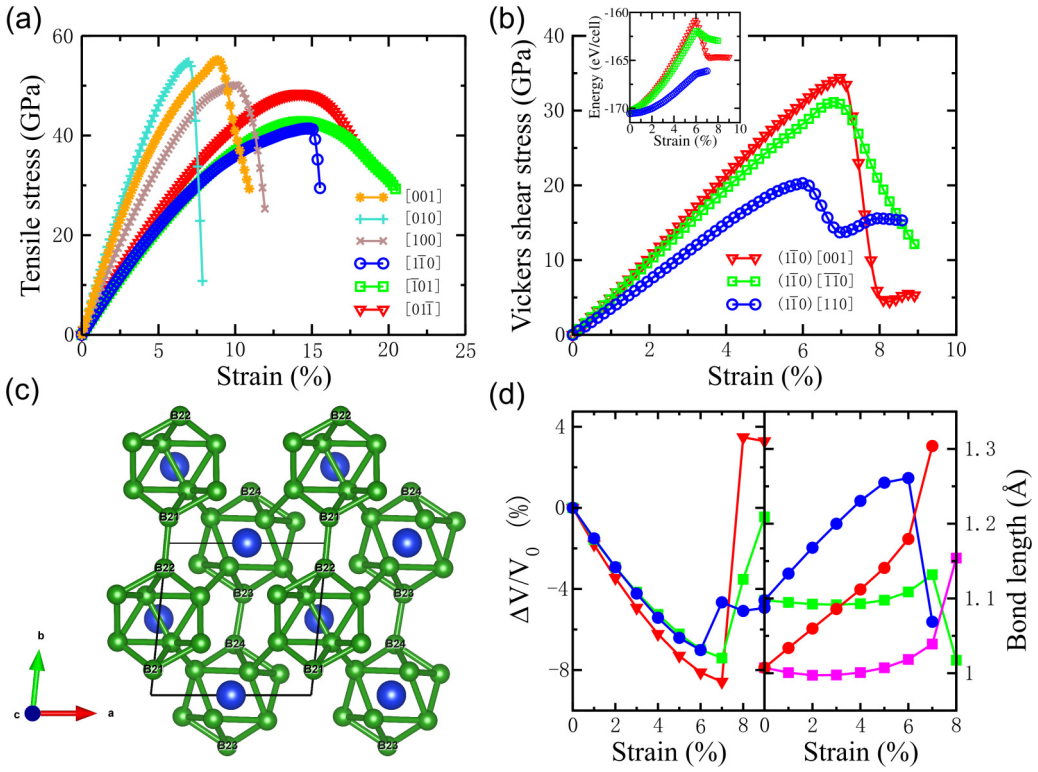

FIG. 4. The stress-strain relationships for orthorhombic SiB_{12}. (a) The uniaxial ideal tensile strains, and (b) the biaxial shear strains under the Vickers-indentation deformations. (c) The structural snapshot at specific indentation strain of 0.06 for the (1$\bar{1}$0) plane shearing along the [110] direction as the blue circle-solid curve shown in (b). (d, left panel) The volume changes with indentation shear along the [001], [$\bar{1}$ $\bar{1}$ 0], and [110] direction for the (1$\bar{1}$0) plane, which are subjected to the same-colored strain-stress curves in (b). The inset in (b) shows the total energy calculated under strains after fully optimizing the cells upon shearing in the (1$\bar{1}$0) plane along the [001], [$\bar{1}\bar{1}$0], and [110] directions. The solid circle and square lines in the right part of (d) exhibit the directional-bond lengths by projecting the B_P–B_P pairs along the (1$\bar{1}$0)[110] and its opposite shearing directions, respectively. Blue and green curves represent the bond length for B23–B24 pair as labeled in (c), red and magenta ones are for B21–B22 bond.

structure has high elastic moduli, displaying values of 188.0 and 221.7 GPa for the bulk and shear modulus, respectively, [76–78]. Using the semiempirical model of Chen *et al.* [79], we estimate the Vickers hardness to be around 54.2 GPa, which is in agreement with the value (∼50.8 GPa) obtained by model of Tian *et al.* [80]. These predictions suggest the potential super hardness of SiB_{12} at ambient conditions. However, no directionally strong interactions exist between icosahedra, suggesting the material may not be able to resist an imposed Vickers indentation strain, which may lead to facile icosahedral deconstruction thus reducing the expected maximum Vickers hardness [81].

To identify the intrinsic Vickers stiffness of our SiB_{12} structure, we impose tensile strains and shear on the structure to simulate the conditions of a Vickers indentation test. We have calculated the stress under uniaxial ideal tensile strains along different directions, as reported in Fig. 4(a). The structure was optimized to reach the lowest stress peak under the tensile strain around 15% along the [1$\bar{1}$0] direction. We therefore choose the (1$\bar{1}$0) plane as the easiest cleavage. By shearing the (1$\bar{1}$0) plane along the [001], [$\bar{1}$ $\bar{1}$ 0], and [110] directions, we have simulated the expected Vickers-indenter deformations under biaxial strains, as shown in Fig. 4(b). The sheared structure under these conditions is depicted in Fig. 4(c). We optimize the shearing snapshot structures.

Under continuous low shear strain, the total energy can be continuous. However, the partial derivative of total energy E with respect to strain component ϵ_{ij} can be discontinuous, especially at a first-order phase transition point, where the cell volume V is discontinuous. After optimizing the SiB_{12} structure, we find E increases with shear strain, reaching a peak value of 6% strain along the [001] and [$\bar{1}\bar{1}$0] directions in the (1$\bar{1}$0) shear plane [inset of Fig. 4(b)]. The energy tends to increase slowly at 6% shear strain for (1$\bar{1}$0)[110] Vickers indentation. At around 6% shear strain, we find the total energy increments for the [001] and [$\bar{1}\bar{1}$0] directions are almost twice as great as that along the [110] direction. On the other hand, the cell can be compressed with decreasing volume V under shear strain. Sudden V increments occur at strains of 6% for (1$\bar{1}$0)[110] and 7% for the (1$\bar{1}$0) [001] and [$\bar{1}\bar{1}$0] directions [Fig. 4(d)], which leads to stress drops [Fig. 4(b)]. These characteristics of energy increment and sudden volume condensation result in the stress-strain curves given in Fig. 4(b). The SiB_{12} structure is predicted to show its lowest stress values under a (1$\bar{1}$0)[110] shear deformation. The stress is estimated to reach a peak value around 20 GPa corresponding to a biaxial shear strain of 6%.

During shearing, we find sudden cell deformations arise, with sudden volumetric expansions, as shown in the left panel of Fig. 4(d). By projecting the boron bond lengths along the

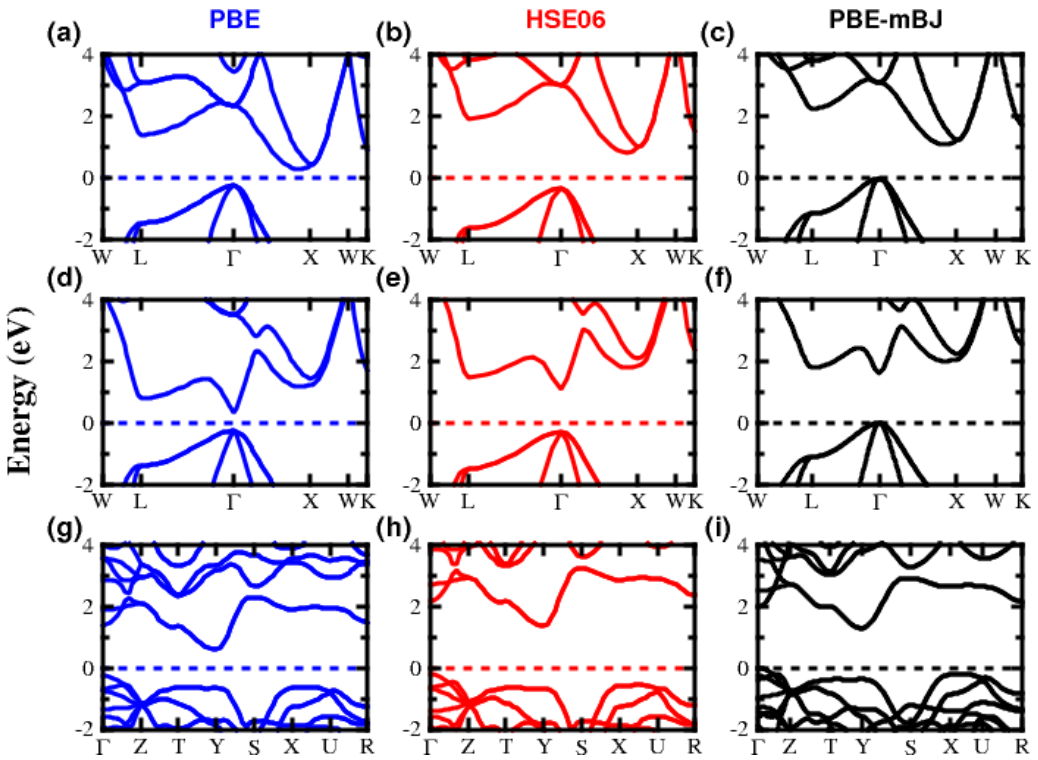

FIG. 5. The band structures for (a)–(c) d-Si, (d)–(f) c-GaAs, and (g)–(i) SiB_{12}. The blue, red, and black band dispersion curves represent the VASP PBE, HSE06, and WIEN2k PBE-mBJ functional method, respectively.

shear system $(1\bar{1}0)[110]$ and along the opposite shear direction, we obtain the directional bond lengths for B_P–B_P pairs between adjacent boron icosahedra. The shorter boron-boron bonds exhibit larger shear stress under $(1\bar{1}0)[\bar{1}\ \bar{1}\ 0]$ deformation than they do under the opposite deformation. The sudden Vickers deformation occurs with a sudden increase in the B21–B22 bond length, as well as a sudden reduction in the B23–B24 bond length. Therefore, we suggest that the boron icosahedra collapse under biaxial shear strains, reducing the intrinsic hardness to around 20 GPa, which is much lower than estimates from the semiempirical models suggest.

E. Electronic properties and optical absorption

The boron icosahedra of our phase form a *Pnnm* orthorhombic SiB_{12} structure. We have explored the influence of the inclusion of interstitial silicon atoms between the boron icosahedra on the electronic properties of this material. The band structure estimation is an important component of our understanding of semiconductor electrical transport properties. It is important to choose an efficient method for evaluating accurate band structures for SiB_{12}.

Here, we compare the PBE, hybrid Heyd-Scuseria-Ernzerhof functional (HSE06) [82] and WIEN2k mBJ exchange potential combined with the PBE functional in VASP. For comparison, we calculated the electronic band structures for well-known diamondlike silicon [d-Si, Figs. 5(a)–5(c)] and cubic GaAs [c-GaAs, Figs. 5(d)–5(f)]. We list the direct and indirect band gaps in Table I, compared with the experimental values. The PBE functional [blue curves in Figs. 5(a) and 5(d)] obviously underestimate the band gaps. The HSE06 functional [red curves in Fig. 5(b) and 5(e)] provides a more accurate estimate of the band gap. However, the HSE06 calculations are time-consuming and computational expensive, especially for large systems.

The mBJ method is an addition to the PBE functional under the GGA. It is computationally cheap and efficient to use the mBJ semilocal functional to correct the electronic band gap for solid-state semiconductors and insulators [83]. We find WIEN2k PBE-mBJ results are comparable with VASP HSE06 bands. The semilocal mBJ potential is defined by $\upsilon_{\chi,\sigma}^{\mathrm{MBJ}}\vec{r} = c\upsilon_{\chi,\sigma}^{\mathrm{BR}}(\vec{r}) + (3c-2)\frac{1}{\pi}\sqrt{\frac{5}{12}}\sqrt{\frac{2t_\sigma}{\rho_\sigma(\vec{r})}}$, where ρ_σ is the electron density, and $\upsilon_{\chi,\sigma}^{\mathrm{BR}}(\vec{r})$ is the Becke-Roussel (BR) potential [83]. The band dispersion curves match well, as shown in Fig. 5(c) and 5(f). In particular, the PBE-mBJ method gives more accurate estimates of the band gaps (Table I) for the d-Si and c-GaAs cells than does HSE06, with lower error (err.) compared to the experimental observations (Table I). Specifically, using PBE-mBJ, we evaluate a band-gap value of 1.15 eV with 1.7% err. for d-Si and 1.64 eV with 7.9% err. for the c-GaAs cell, relative to the experimentally observed values for d-Si of 1.17 eV [28] and c-GaAs of 1.52 eV [83]. The PBE-mBJ band-gap results are better than the computationally demanding HSE06 calculations (1.10 eV with 6.0% err. for d-Si, 1.35 eV with 11.2% for c-GaAs). Therefore, we have adopted WIEN2k PBE-mBJ calculations to determine the electronic band structure of SiB_{12} and related materials. In Figs. 5(g)–5(i), we compare the band dispersions for SiB_{12} estimated by PBE, HSE06, and PBE-mBJ methods.

Our PBE-mBJ calculations show that the SiB_{12} *Pnnm* phase is a semiconductor with a small indirect band gap of

TABLE I. The band gap (eV) and error (%) in relative to the experimental values (exp.).

Compound \ Functional	PBE (eV) Err. (%)	HSE (eV) Err. (%)	PBE-mbj (eV) Err. (%)	Exp. (eV)
d-Si	1.02	1.10	1.15	1.17 [28]
	12.8	6.0	1.7	
c-GaAs	0.59	1.35	1.64	1.52 [83]
	61.2	11.2	7.9	
SiB_{12}	0.82	1.56	1.28	–
	–	–	–	

around 1.3 eV [Fig. 6(a)]. The valence band maximum (VBM) and conduction band minimum (CBM) points are located at Γ and Y points of the Brillouin zone, respectively. Double degeneracy occurs along the Z–R direction at energy levels of 1–3 and −1–0 eV for the conduction and valence bands respectively. The flat valence band broadens with a hole of large effective mass along the T–Y and X–U directions of the Brillouin zone. These intrinsic band characteristics are beneficial for electron inter-band transitions from valence to conduction bands under visible light. The atomic pDOS in the right panel of Fig. 6(a), shows that boron $2p$ orbital electrons predominantly contribute to both valence and conduction bands. The electron excitation has a small contribution to the free energy for the indirect band gap of SiB_{12}.

Based on the proposed band structures given by WIEN2k PBE-mBJ (Fig. 5), we further performed optical-absorption calculations for solid *Pnnm* SiB_{12} using the linearized augmented plane wave (LAPW) method [85]. We present the absorption coefficient (α) as a function of photon energy in Fig. 6(b). However, we did not consider the electron indirect transition between the occupied and unoccupied states, which involves absorption and release of phonons. Nevertheless, using the LAPW method employed in WIEN2k code, we calculate interband absorption coefficients (α) for SiB_{12}, compared with cubic GaAs (c-GaAs) and diamondlike silicon (d-Si). Values of α for c-GaAs and d-Si are in good agreement with the experimental observations across the visible spectrum, as shown in Fig. 6(b). This validates the use of the WIEN2k PBE-mBJ method in estimating such optical properties for direct and indirect semiconductors.

According to the sum rules for Bloch electron transition from an occupied state to empty state, the imaginary components (ε_2^{ij}) of the interband complex dielectric tensor vary with incident photon frequency ν. This is calculated as $\varepsilon_2^{ij}(\nu) = \frac{e^2}{\pi m^2 \nu^2} \sum_{\vec{k}nn'\sigma} \langle \vec{k}n\sigma | p_i | \vec{k}n'\sigma \rangle \langle \vec{k}n'\sigma | p_j | \vec{k}n\sigma \rangle \times (f_{\vec{k}n} - f_{\vec{k}n'}) \delta(E_{\vec{k}n'} - E_{\vec{k}n} - h\nu)$ [85]. Here, m and e represent electron mass and quantity, $\vec{P}$ is the momentum operator, $|\vec{k}n\sigma\rangle$ is the eigenstate of energy $E_{\vec{k}n}$, $\vec{k}$ is the wave vector, and $f_{\vec{k}n}$ is Fermi-Dirac distribution function. We obtain the real part (ε_1) of the dielectric function from the Kramers-Kronig transformation $\varepsilon_1^{ij}(\nu) = \delta_{ij} + \frac{2}{\pi} \wp \int_0^\infty \frac{\nu' \varepsilon_2^{ij}(\nu')}{\nu'^2 - \nu^2} d\nu'$. The

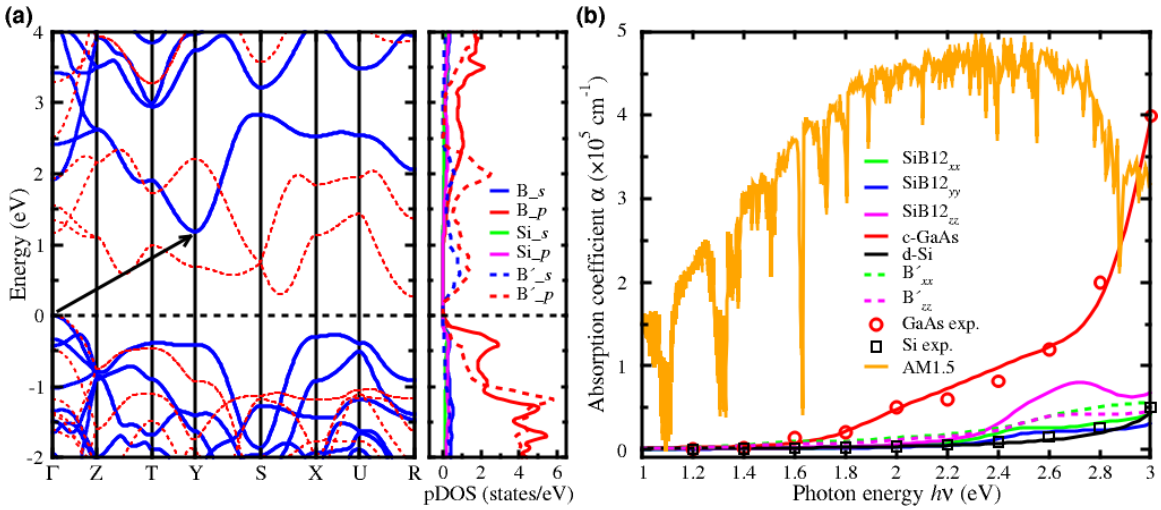

FIG. 6. The electronic structures of *Pnnm* SiB_{12} and its absorption features in the visible-light range. (a) The electronic band structure (left panel) and partial density of state (pDOS, right panel), and (b) the optical properties compared to other typical optoelectronic materials, specifically, cubic GaAs (c-GaAs) and diamondlike silicon (d-Si) cells. We used the WIEN2k code to calculate the absorption efficiency with the mBJ potential. Removing the silicon atoms, dashed color lines in (a) and (b) show the corresponding band structure, pDOS and optical absorption for pure icosahedral B_{12} lattice (B'). The black dashed line in (a) represents the maximum energy level of the valence bands. For comparison, we select the optical-absorption data for c-GaAs (red square) and d-Si (black square) cells at 300 K from the primary literature of Blakemore [12] and Green *et al.* [84], respectively. The yellow solid line in (b) describes the AM1.5 standard solar spectra in arbitrary units.

absorption coefficient (α^{ii}) is then estimated by $\alpha^{ii}(\nu) = \frac{\sqrt{2}\nu}{c}[\sqrt{\varepsilon_1^{ii2}(\nu) + \varepsilon_2^{ii2}(\nu)} - \varepsilon_1^{ii}(\nu)]^{1/2}$, where c is light speed.

The first two ε_2 peaks of SiB_{12} are observed at around 2.7 and 3.1 eV, compared with 3.0 and 4.2 eV for c-GaAs and 3.5, 5.0 eV for d-Si solar cells (SM Fig. S4). This demonstrates that the optical absorption coefficient, α, of SiB_{12} is higher than that of d-Si and comparable to that of c-GaAs solar cells in the visible light range. The magnitude of α of SiB_{12} is enhanced at an incident photon energy below 3.0 eV, with total overlap with air mass (AM) 1.5 absorption solar spectral irradiance [86,87]. This indicates the good absorption efficiency as a solar cell.

Absorption of light increases at photon energy levels above 1.6 eV for SiB_{12} structure, which likely results from the dramatic DOS enhancement around energy levels of −0.3 eV below the VBM. Based on accurate full-potential LAPW band-structure calculations, the absorption of light by *Pnnm* SiB_{12} is expected to be much more anisotropic for *xx* and *zz* components, certainly more so than d-Si photovoltaic material in the photon energy range of 2.0–3.0 eV. In particular, the absorption coefficient *zz* for SiB_{12} reaches a maximum value of around 0.8×10^5 cm^{-1} at a photon energy level of 2.7 eV, which is comparable to that of c-GaAs [12]. We suggest that SiB_{12} has better and more efficient absorption of the sunlight than that of a diamondlike silicon solar cell.

Therefore, we suggest that *Pnnm* SiB_{12} is a good absorber across the visible light range. The photon absorption appears to be associated with the boron icosahedral structure, since we calculated that the silicon-free pure boron material retains similar band characteristics as depicted by the red dashed lines in Fig. 6(a).

F. Thermoelectric properties

In addition to their photoabsorption characteristics, the unique structure and electronic properties of our predicted SiB_{12} phase may also imbue superior thermoelectric performance. For example, the dodecahedral cage structure and large differential electric DOS around the Fermi energy have previously been associated with a superior Seebeck effect (S) and low thermal conductivity (κ_L) [5,11,14,88], which are key merit indices for good thermoelectric materials. The low band gap of 1.3 eV and good structural stability displayed by semiconducting SiB_{12} inspire us to study potential thermoelectric applications of this phase over a wide range of possible working temperatures.

The dimensionless thermoelectric figure of merit, $ZT = \frac{S^2\sigma T}{\kappa_L + \kappa_e}$, determines the efficiency of heat-to-electric conversion for a thermoelectric material. Here, σ, κ_L and κ_e, and T correspond to the electrical conductivity, lattice and charge-carrier thermal conductivity, and absolute working temperature, respectively. The magnitude of S closely depends upon the effective mass and carrier concentration (n), which are in turn determined by the electronic band structure around the Fermi energy [89]. We have evaluated the charge-carrier transport properties of *Pnnm* SiB_{12} using the BOLTZTRAP package [65], based on calculations of the band-energy eigenvalues providing by the mBJ functional employed in the WIEN2k code. As Fig. 7(a) demonstrates, for a hole carrier, the Seebeck coefficient, S, increases from 150 to 400 μVK^{-1} for a positive value of n of 1×10^{20} cm^{-3} as the temperature increases from 300 to 1100 K respectively. The absolute value of S with negative n is less than that for the equivalent magnitude positive n, indicating that *Pnnm* SiB_{12} shows the *p*-type Seebeck effect.

The flat VBM bands at energy levels of −1.0 eV along the *T*–*Y* and *X*–*U* directions of the Brillouin zone suggest a much larger DOS for valence bands than that for CBM at the *Y* point. Such obvious DOS differences result in the larger effective mass of a hole carrier than that of an electron, however, leading to a smaller σ for positive n than that expected for negative n [see SM Fig. S5(a)]. The electrical conductivity σ reaches around 10^5 at negative $n = 1 \times 10^{20}$ which is much larger than β-boron [26], and comparable to that of TaFeSb-based half-Heusler systems [90]. With an appropriate constant relaxation time ($\tau = 10^{-14}$ s) for bulk materials [91–97], we have calculated the power factor ($PF = S^2\sigma$) taking into account the carrier electrical conductivity, as shown in Fig. 7(b). The PF of hole carriers is estimated to be larger than that of an electron, which increases with the temperature.

The lattice thermal conductivity (κ_L) in particular plays an important role in thermoelectric performance at room temperature. Reducing κ_L has been reported to be an effective way to lower heat transport and improving the ZT value [15]. However, the third-order interatomic force constants are necessary to perform SHENGBTE [66]. We find low values of lattice thermal conductivity, ranging from 19.2 $Wm^{-1}K^{-1}$ at 300 K to 5.0 $Wm^{-1}K^{-1}$ at 1100 K [Fig. 7(c)]. These are lower than the thermal conductivity of pure β boron, of around 30 to 10 $Wm^{-1}K^{-1}$ over temperature ranges of 300–1000 K [26], but higher than those of $CaMg_2Sb_2$ (4.5 $Wm^{-1}K^{-1}$@300 K). However, κ_L is much lower than bulk diamond (1700 $Wm^{-1}K^{-1}$) or of diamondlike silicon (100 $Wm^{-1}K^{-1}$) at 300 K [98]. We have calculated the normalized cumulative thermal conductivity κ_C/κ_L as a function of phonon frequency at 300 K [Fig. 7(d)]. Over 80% of the lattice thermal conductivity κ_L is contributed by phonons with frequency below 400 cm^{-1}, as the black dashed line shows. Considering the cell size effects, we calculate the κ_L for nanowires formed along the [010] direction for different diameters ranging from 10 to 10^4 nanometers (nm) [Fig. 7(e)]. κ_L is found to be greatly reduced when the cell size is limited to less than 100 nm.

We find the total scattering rate tends to increase with increasing temperature [see SM Fig. S6(b)]. Strong phonon scattering occurs at frequencies around 300 and 400 cm^{-1}, where group velocities υ_g reach around 7 km/s [SM Fig. S5(c)], which is much larger than the narrow band-gap thermoelectric Bi_2Se_3 (∼1.62 km/s) [99]. We suggest that the noticeable intensification of the total scattering rate originates from the vibrations of the silicon atoms in the open channel sites between boron icosahedra, as Figs. 3(c) and 3(g)–3(i) indicate. The silicon atom may show large amplitude vibrational motions that can effectively scatter any low-frequency phonons, behaving somewhat akin to the "rattling" guest atoms seen previously in phonon-glass electron crystals [100]. The electrical thermal conductivity (κ_e) tends to depend more significantly on the magnitude of ZT value at temperatures above 500 K [see SM Fig. S5(d)].

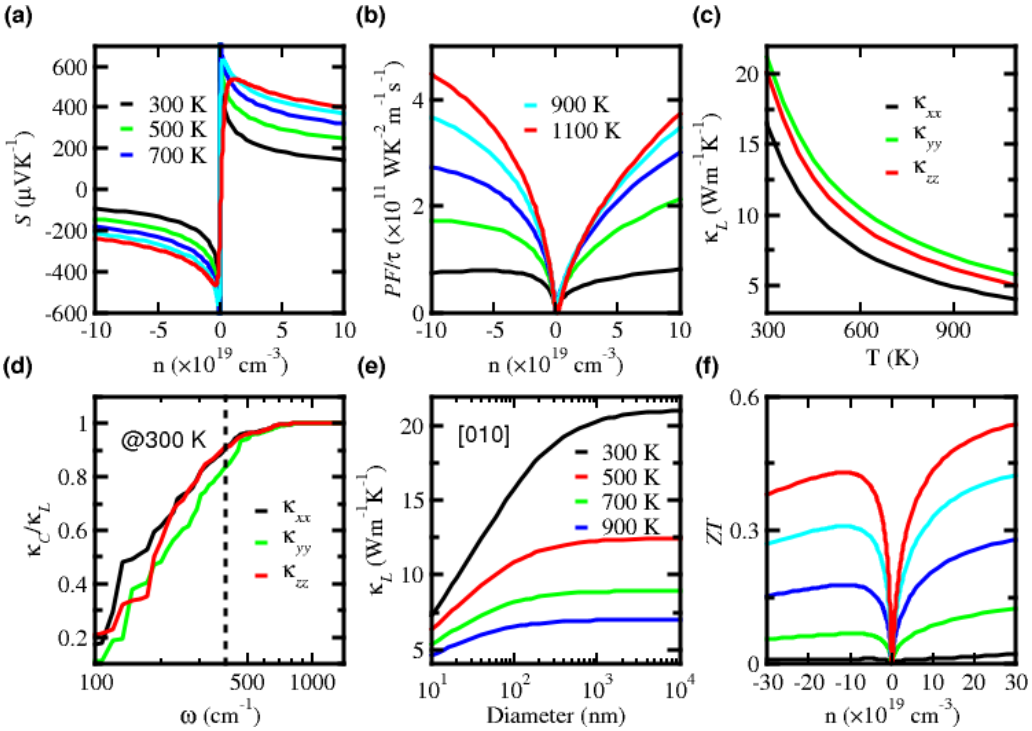

FIG. 7. Electrical transport and lattice thermal properties for *Pnnm* SiB_{12}. (a) The Seebeck coefficient (S) and (b) power factor ($PF = S^2\sigma$) at constant relaxation time (τ) are shown as a function of carrier concentration (n). (c) The lattice thermal conductivity (κ_L) versus temperature (T) for xx, yy, and zz components in *Pnnm* SiB_{12}. (d) The normalized cumulative thermal conductivity κ_C/κ_L with phonon frequency ω at 300 K. (e) κ_L for nanowires along [010] growth direction at temperatures from 300 to 900 K. (f) The calculated temperature-dependent figure of merit (ZT) versus carrier concentration n. The constant $\tau = 10^{-14}$ s is appropriate for applications in many systems [91–97].

As a result, ZT is estimated to increase with working temperature over the range 300–1100 K, as shown in Fig. 7(f). We find large electrical conductivity and low lattice thermal conductivity for SiB_{12}, result in a very large thermoelectric ZT value of 0.56 at 1100 K. This is much better than that of pure boron or of the boron oxide B_6O (best ZT of 0.17 at 1200 ° C) [26], and is almost twice as high as that of the benchmark thermoelectric Bi_2Se_3 (ZT of 0.3) [97].

IV. CONCLUSIONS

We have applied crystal structure search methods to explore stable icosahedral silicon borides under pressure. An orthorhombic SiB_{12} structure with space group *Pnnm* is found to be stable at around 20 GPa and quenchable to ambient pressure. This structure is composed of boron-icosahedral clusters with interstitial with silicon atoms, and exhibits very good thermal and dynamic stability. For example, our AIMD simulations show that the phonon dispersion branches of SiB_{12} are found to all have positive frequencies at ambient pressure and finite temperatures. The icosahedron clusters in the structure are seen to remain intact, even to temperatures as high as 2000 K. Calculations of electron localization functions reveal strong covalent bonding between the boron icosahedra. Very weak noncovalent interactions are seen around the silicon atoms, from reduced density gradient analysis. Calculations of the Vickers-indentation deformation hardness suggest that this structure is stiff to shear and has an intrinsic Vickers hardness of around 20 GPa. By performing the accurate all-electron band-structure calculations, we find that the SiB_{12} structure is semiconducting with a small indirect band gap of around 1.3 eV. It shows a good optical absorption coefficient across the visible light range. Additionally, the guest silicon atom intensifies the scattering rate and imbues the SiB_{12} structure with a good Seebeck effect and low lattice thermal conductivity. Therefore, our work suggests that SiB_{12} is a hard semiconducting compound with multifunctional properties. Specifically, the superior photovoltaic and thermoelectric performance of this compound makes it potentially useful for renewable energy production, with enhanced total photovoltaic conversion efficiency. We anticipate that the predictions that we have outlined here will stimulate experimentalists to synthesize and further apply this interesting compound.

ACKNOWLEDGMENTS

K.X. acknowledges the financial support from the National Natural Science Foundation of China under Grant No. 12004185, The Natural Science Foundation of the Jiangsu Higher Education Institutions of China under Grant No. 20KJB140016, the Scientific Research Start-up Funds of Nanjing Forestry University (163101110), and the Project funded by China Postdoctoral Science Foundation under Grant No. 2019M651767. J.S. thanks the financial support from the National Key R&D Program of China under Grant No. 2016YFA0300404, the National Natural Science Foundation of China under Grants No. 11974162 and

No. 11834006, and the Fundamental Research Funds for the Central Universities. The numerical calculations in this paper were performed on the computing facilities in the High-Performance Computing Facility of Nanjing Forestry University, the High-Performance Computing Center of Collaborative Innovation Center of Advanced Microstructures, and the High-Performance Computing Center (HPCC) of Nanjing University.

[1] K. Wilhelm, W. Curdt, E. Marsch, U. Schuhle, P. Lemaire, A. Gabriel, J. C. Vial, M. Grewing, M. C. E. Huber, S. D. Jordan, A. I. Poland, R. J. Thomas, M. Kuhne, J. G. Timothy, D. M. Hassler, and O. H. W. Siegmund, Sol. Phys. **162**, 189 (1995).
[2] M. Wild, H. Gilgen, A. Roesch, A. Ohmura, C. N. Long, E. G. Dutton, B. Forgan, A. Kallis, V. Russak, and A. Tsvetkov, Science **308**, 847 (2005).
[3] E. Radziemska, Renew. Energy **28**, 1 (2003).
[4] D. Kraemer, B. Poudel, H.-P. Feng, J. C. Caylor, B. Yu, X. Yan, Y. Ma, X. Wang, D. Wang, A. Muto, K. McEnaney, M. Chiesa, Z. Ren, and G. Chen, Nat. Mater. **10**, 532 (2011).
[5] J. He and T. M. Tritt, Science **357**, 1369 (2017).
[6] T. T. Chow, Appl. Energyy **87**, 365 (2010).
[7] T. Chen, G. H. Guai, C. Gong, W. Hu, J. Zhu, H. Yang, Q. Yan, and C. M. Li, Energy Environ. Sci. **5**, 6294 (2012).
[8] T. Liu, C. Wang, J. Hou, C. Zhang, H. Chen, H. He, N. Wang, H. Wu, and G. Cao, Small **12**, 5146 (2016).
[9] P. Huen and W. A. Daoud, Renew. Sustain Energy Rev. **72**, 1295 (2017).
[10] M. A. Green and S. P. Bremner, Nat. Mater. **16**, 23 (2017).
[11] B. Hinterleitner, I. Knapp, M. Poneder, Y. Shi, H. Mu¨ller, G. Eguchi, C. Eisenmenger-Sittner, M. Stöger-Pollach, Y. Kakefuda, N. Kawamoto, Q. Guo, T. Baba, T. Mori, S. Ullah, X.-Q. Chen, and E. Bauer, Nature (London) **576**, 85 (2019).
[12] J. S. Blakemore, J. Appl. Phys. **53**, R123 (1982).
[13] G. J. Snyder and E. S. Toberer, Nat. Mater. **7**, 105 (2008).
[14] T. Tadano, Y. Gohda, and S. Tsuneyuki, Phys. Rev. Lett. **114**, 095501 (2015).
[15] Z. Chen, X. Zhang, and Y. Pei, Adv. Mater. **30**, 1705617 (2018).
[16] Z. Chen, X. Zhang, S. Lin, L. Chen, and Y. Pei, Natl. Sci. Rev. **5**, 888 (2018).
[17] M. I. Eremets, V. V. Struzhkin, H. Kwang Mao, and R. J. Hemley, Science **293**, 272 (2001).
[18] A. R. Oganov, J. Chen, C. Gatti, Y. Ma, Y. Ma, C. W. Glass, Z. Liu, T. Yu, O. O. Kurakevych, and V. L. Solozhenko, Nature (London) **457**, 863 (2009).
[19] Q. An, K. M. Reddy, K. Y. Xie, K. J. Hemker, and W. A. Goddard, Phys. Rev. Lett. **117**, 085501 (2016).
[20] X.-F. Zhou, X. Dong, A. R. Oganov, Q. Zhu, Y. Tian, and H.-T. Wang, Phys. Rev. Lett. **112**, 085502 (2014).
[21] X.-F. Zhou, A. R. Oganov, Z. Wang, I. A. Popov, A. I. Boldyrev, and H.-T. Wang, Phys. Rev. B **93**, 085406 (2016).
[22] G. Akopov, M. T. Yeung, and R. B. Kaner, Adv. Mater. **29**, 1604506 (2017).
[23] K. Xia, M. Ma, C. Liu, H. Gao, Q. Chen, J. He, J. Sun, H.-T. Wang, Y. Tian, and D. Xing, Mater. Today Phys. **3**, 76 (2017).
[24] X.-L. He, X. Dong, Q. Wu, Z. Zhao, Q. Zhu, A. R. Oganov, Y. Tian, D. Yu, X.-F. Zhou, and H.-T. Wang, Phys. Rev. B **97**, 100102(R) (2018).
[25] Z. Yuan, M. Xiong, and D. Yu, Phys. Lett. A **384**, 126075 (2020).
[26] G. Slack and K. Morgan, Solid State Sci. **47**, 43 (2015).
[27] T. L. Aselage, J. Mater. Res. **13**, 1786 (1998).
[28] D. Y. Kim, S. Stefanoski, O. O. Kurakevych, and T. A. Strobel, Nat. Mater. **14**, 169 (2015).
[29] Q. Wang, B. Xu, J. Sun, H. Liu, Z. Zhao, D. Yu, C. Fan, and J. He, J. Am. Chem. Soc. **136**, 9826 (2014).
[30] J. Wu, H. Gao, K. Xia, D. Xing, and J. Sun, Appl. Phys. Lett. **111**, 173904 (2017).
[31] D. W. Lee, K. H. Kim, J. Matsushita, K. Niihara, K. H. Auh, and K. B. Shim, J. Ceram. Process. Res. **3**, 182 (2002).
[32] L.-C. Chen, P.-Q. Chen, W.-J. Li, Q. Zhang, V. V. Struzhkin, A. F. Goncharov, Z. Ren, and X.-J. Chen, Nat. Mater. **18**, 1321 (2019).
[33] N. V. Morozova, I. V. Korobeinikov, and S. V. Ovsyannikov, J. Appl. Phys. **125**, 220901 (2019).
[34] K. Xia, H. Gao, C. Liu, J. Yuan, J. Sun, H.-T. Wang, and D. Xing, Sci. Bull. **63**, 817 (2018).
[35] H. Gao, J. J. Wang, Z. P. Guo, and J. Sun, NPJ Comput. Mater. **6**, 143 (2020).
[36] C. Liu, J. Y. Shi, H. Gao, J. J. Wang, Y. Han, X. C. Lu, H.-T. Wang, D. Xing, and J. Sun, Phys. Rev. Lett. **126**, 035701 (2021).
[37] Q. Gu, D. Xing, and J. Sun, Chin Phys. Lett. **36**, 097401 (2019).
[38] C. Liu, H. Gao, Y. Wang, R. J. Needs, C. J. Pickard, J. Sun, H.-T. Wang, and D. Xing, Nat. Phys. **15**, 1065 (2019).
[39] C. Liu, H. Gao, A. Hermann, Y. Wang, M. Miao, C. J. Pickard, R. J. Needs, H.-T. Wang, D. Xing, and J. Sun, Phys. Rev. X **10**, 021007 (2020).
[40] H. Gao, C. Liu, A. Hermann, R. J. Needs, C. J. Pickard, H.-T. Wang, D. Xing, and J. Sun, Natl. Sci. Rev. **7**, 1540 (2020).
[41] K. Xia, X. Zheng, J. Yuan, C. Liu, H. Gao, Q. Wu, and J. Sun, J. Phys. Chem. C **123**, 10205 (2019).
[42] K. Xia, J. Yuan, X. Zheng, C. Liu, H. Gao, Q. Wu, and J. Sun, J. Phys. Chem. Lett **10**, 6166 (2019).
[43] J. P. Perdew, K. Burke, and M. Ernzerhof, Phys. Rev. Lett. **77**, 3865 (1996).
[44] P. E. Blochl, Phys. Rev. B **50**, 17953 (1994).
[45] G. Kresse and J. Furthmuller, Phys. Rev. B **54**, 11169 (1996).
[46] A. Togo, L. Chaput, I. Tanaka, and G. Hug, Phys. Rev. B **81**, 174301 (2010).
[47] A. Togo and I. Tanaka, Scr. Mater. **108**, 1 (2015).
[48] A. D. Becke and K. E. Edgecombe, J. Chem. Phys. **92**, 5397 (1990).
[49] E. R. Johnson, S. Keinan, P. Mori-Sanchez, J. Contreras-Garcia, A. J. Cohen, and W. Yang, J. Am. Chem. Soc. **132**, 6498 (2010).
[50] A. Otero-de-la Roza, E. R. Johnson, and V. Luana, Comput. Phys. Commun. **185**, 1007 (2014).
[51] W. Humphrey, A. Dalke, and K. Schulten, J. Mol. Graph. Model. **14**, 33 (1996).

[52] D. Roundy, C. R. Krenn, M. L. Cohen, and J. W. Morris, Phys. Rev. Lett. **82**, 2713 (1999).

[53] B. Li, H. Sun, and C. Chen, Nat. Commun. **5**, 4965 (2014).

[54] F. Tran and P. Blaha, Phys. Rev. B **83**, 235118 (2011).

[55] P. Blaha, K. Schwarz, P. Sorantin, and S. Trickey, Comput. Phys. Commun. **59**, 399 (1990).

[56] M. Parrinello and A. Rahman, Phys. Rev. Lett. **45**, 1196 (1980).

[57] C. L. Brooks, J. Solution Chem. **18**, 99 (1989).

[58] N. Shulumba, O. Hellman, and A. J. Minnich, Phys. Rev. B **95**, 014302 (2017).

[59] W. G. Hoover, A. J. C. Ladd, and B. Moran, Phys. Rev. Lett. **48**, 1818 (1982).

[60] D. J. Evans, J. Chem. Phys. **78**, 3297 (1983).

[61] M. P. Allen and D. J. Tildesley, *Computer Simulation of Liquids* (Oxford University Press, New York, 1991).

[62] M. Parrinello and A. Rahman, J. Appl. Phys. **52**, 7182 (1981).

[63] F. Eriksson, E. Fransson, and P. Erhart, Adv. Theor. and Simul. **2**, 1800184 (2019).

[64] I. Errea, M. Calandra, and F. Mauri, Phys. Rev. B **89**, 064302 (2014).

[65] G. K. Madsen and D. J. Singh, Comput. Phys. Comm. **175**, 67 (2006).

[66] W. Li, J. Carrete, N. A. Katcho, and N. Mingo, Comput. Phys. Commun. **185**, 1747 (2014).

[67] See Supplemental Material at http://link.aps.org/supplemental/10.1103/PhysRevMaterials.5.115402 for more details on the lattice parameters, elastic constants, Bader charge and macroscopic modulus of SiB_{12} structure, the Gibbs free energy change with volume variance, the AIMD simulations, the dielectric function calculation and the electric transportation properties.

[68] R. F. W. Bader, *Atoms in Molecules: A Quantum Theory.* (Clarendon, Oxford, 1990).

[69] J. Navas, A. Sánchez-Coronilla, J. J. Gallardo, N. C. Hernández, J. C. Piñero, R. Alcántara, C. Fernández-Lorenzo, D. M. D. los Santos, T. Aguilar, and J. Martín-Calleja, Nanoscale **7**, 6216 (2015).

[70] G. J. O. Beran, Chem. Rev. **116**, 5567 (2016).

[71] H. Kasai, K. Tolborg, M. Sist, J. Zhang, V. R. Hathwar, M. Ø. Filsø, S. Cenedese, K. Sugimoto, J. Overgaard, E. Nishibori, and B. B. Iversen, Nat. Mater. **17**, 249 (2018).

[72] I. Errea, M. Calandra, and F. Mauri, Phys. Rev. Lett. **111**, 177002 (2013).

[73] I. Errea, M. Calandra, C. J. Pickard, J. Nelson, R. J. Needs, Y. Li, H. Liu, Y. Zhang, Y. Ma, and F. Mauri, Phys. Rev. Lett. **114**, 157004 (2015).

[74] T. Chen, D. Shao, P. Lu, X. Wang, J. Wu, J. Sun, and D. Xing, Phys. Rev. B **98**, 144105 (2018).

[75] O. Hellman, P. Steneteg, I. A. Abrikosov, and S. I. Simak, Phys. Rev. B **87**, 104111 (2013).

[76] G. V. Sin'ko and N. A. Smirnov, J. Phys.: Condens. Matter **14**, 6989 (2002).

[77] J. G. Berryman, J. Mech. Phys. Solids **53**, 2141 (2004).

[78] G. Grimvall, B. Magyari-Kope, V. Ozolins, and K. A. Persson, Rev. Mod. Phys. **84**, 945 (2012).

[79] X.-Q. Chen, H. Niu, D. Li, and Y. Li, Intermetallics **19**, 1275 (2011).

[80] Y. Tian, B. Xu, and Z. Zhao, Int. J. Refract. Metall. H. **33**, 93 (2012).

[81] Q. An, Phys. Rev. B **95**, 100101(R) (2017).

[82] A. V. Krukau, O. A. Vydrov, A. F. Izmaylov, and G. E. Scuseria, J. Chem. Phys. **125**, 224106 (2006).

[83] F. Tran and P. Blaha, Phys. Rev. Lett. **102**, 226401 (2009).

[84] M. A. Green and M. J. Keevers, Prog. Photovoltaics **3**, 189 (1995).

[85] C. Ambrosch-Draxl and J. O. Sofo, Comput. Phys. Commun. **175**, 1 (2006).

[86] M. Hybertsenand S. Louie, Phys. Rev. Lett. **55**, 1418 (1985).

[87] B. D. Malone, S. G. Louie, and M. L. Cohen, Phys. Rev. B **81**, 115201 (2010).

[88] C. J. Perez, V. J. Bates, and S. M. Kauzlarich, Inorg. Chem. **58**, 1442 (2018).

[89] X. He, D. J. Singh, P. Boon-on, M.-W. Lee, and L. Zhang, J. Am. Chem. Soc. **140**, 18058 (2018).

[90] H. T. Zhu, J. Mao, Y. W. Li, J. F. Sun, Y. M. Wang, Q. Zhu, G. N. Li, Q. C. Song, J. W. Zhou, and Y. H. Fu, Nat. Commun. **10**, 270 (2019).

[91] J. Yang, H. Li, T. Wu, W. Zhang, L. Chen, and J. Yang, Adv. Funct. Mater. **18**, 2880 (2008).

[92] D. Parker and D. J. Singh, J. Appl. Phys. **108**, 083712 (2010).

[93] M.-S. Lee, F. P. Poudeu, and S. D. Mahanti, Phys. Rev. B **83**, 085204 (2011).

[94] B.-T. Wang, M. A. Petrukhina, and E. R. Margine, Carbon **94**, 174 (2015).

[95] B. Dong, Z. Wang, N. T. Hung, A. R. Oganov, T. Yang, R. Saito, and Z. Zhang, Phys. Rev. Mater. **3**, 013405 (2019).

[96] J. Zhang, L. Song, and B. B. Iversen, NPJ Comput. Mater. **5**, 76 (2019).

[97] S. Huang, Z. Wang, R. Xiong, H. Yu, and J. Shi, Nano Energy **62**, 212 (2019).

[98] W. Li, N. Mingo, L. Lindsay, D. A. Broido, D. A. Stewart, and N. A. Katcho, Phys. Rev. B **85**, 195436 (2012).

[99] S. Y. Wang, Y. X. Sun, J. Yang, B. Duan, L. H. Wu, W. Q. Zhang, and J. H. Yang, Energy Environ. Sci. **9**, 3436 (2016).

[100] T. Takabatake, K. Suekuni, T. Nakayama, and E. Kaneshita, Rev. Mod. Phys. **86**, 669 (2014).